CrystEngComm

PAPER

View Article Online
View Journal

Cite this: DOI: 10.1039/c9ce00039a

A novel strategy for the synthesis of hollow Pt–Cu tetradecahedrons as an efficient electrocatalyst toward methanol oxidation†

Ruopeng Zhao,‡[ab] Gengtao Fu, ‡[d] Zhijing Chen,[a] Yawen Tang, *[c] Yi Wang *[be] and Shaoming Huang *[a]

Received 8th January 2019,
Accepted 30th January 2019

DOI: 10.1039/c9ce00039a

rsc.li/crystengcomm

Various bimetallic hollow structures have been widely reported in literature for their excellent catalytic performance. However, researchers still face challenges in tailoring the structures by an efficient and economical method. Herein, we reported a novel, facile and efficient synthetic strategy to synthesize platinum–copper alloy tetradecahedrons (Pt–Cu TNs) with hollow structures by using tetradecahedral Cu_2O as a starting template; we also controlled the thickness of the shell and Pt/Cu ratio. The structure and the formation mechanism of Pt–Cu TNs were investigated in detail. Such Pt–Cu TNs exhibited significantly enhanced activity, stability and CO tolerance ability for the methanol oxidation reaction (MOR) compared with a commercial Pt black catalyst. This can be attributed to their higher specific surface area, easy access for reactants to the catalyst surface, rough surfaces, and the synergistic effect between Pt and Cu.

Introduction

To meet the energy demands in the future, fuel cells, especially direct methanol fuel cells (DMFCs), have received extensive attention in recent decades owing to their significant advantages of high energy conversion efficiency, convenient fuel storage, fuel safety, low operation and low pollutant emissions.[1–8] The efficiency of DMFCs greatly depends on the electrocatalyst of the anode that operates the methanol oxidation reaction (MOR).[9,10] Even though platinum (Pt) is the most common electrocatalyst employed for MOR, its scarcity, high cost and poor anti-CO poisoning limit its wide applications. Therefore, it is important to develop high-performance and cost-effective alternatives for the anode catalyst for MOR.

A large number of literatures have reported that Pt alloyed with a nonprecious metal not only decreases the usage of Pt but also significantly enhances its catalytic activity through the electronic effect and the synergistic effect between different components.[11–17] In addition to composition, the control of morphology and structure also provides an important route to tailor the catalytic properties.[18–23] Among various well-defined Pt-based materials, Pt-based nanocrystals with hollow features such as cages and frames have attracted considerable attention due to their high specific surface area, good stability and superior connectivity.[24–27] More specifically, a hollow structure can reduce the usage of precious Pt and resistance to form close-packed structures. The collision frequency between active species and reaction sites can be increased for its superior connectivity, leading to enhanced catalytic performance.[28]

Inspired by such advantages, various strategies including chemical etching, galvanic displacement and Kirkendall effect have been employed for the design and synthesis of hollow Pt-based nanostructures. For instance, Xia and co-workers synthesized hollow Pt–Ag alloy nanocages through a galvanic replacement reaction using Ag as the template.[29] Shen and co-workers prepared concave Pt–Cu octopod nanoframes by the stirring-assisted solvothermal method with cetyltrimethylammonium bromide as a surfactant and a structure-directing agent at a high temperature.[30] Huang and co-workers achieved Pt–Ni nanoframes in an organic solution system at a high temperature.[31] Linic and co-workers applied a light-mediated method to synthesize hollow Ag–Pt alloy structures.[32] However, the above catalysts were prepared in extreme conditions such as high temperatures, high-energy gamma radiation or organic solution systems for the intrinsic immiscibility of metals, which are neither environmentally friendly nor cost-effective. Therefore, the development of a

[a] School of Materials and Energy, Guangdong University of Technology, Guangzhou, 510006, PR China. E-mail: smhuang@wzu.edu.cn
[b] Wenzhou Institute of Biomaterials and Engineering, Chinese Academy of Sciences, Wenzhou, 325000, PR China. E-mail: wangyi@wibe.ac.cn
[c] Jiangsu Key Laboratory of New Power Batteries, Jiangsu Collaborative Innovation Center of Biomedical Functional Materials, School of Chemistry and Materials Science, Nanjing Normal University, Nanjing 210023, PR China. E-mail: tangyawen@njnu.edu.cn
[d] School of Chemical and Biomedical Engineering, Nanyang Technology University, Singapore, 637459, Singapore
[e] School of Ophthalmology and Optometry, Eye Hospital, School of Biomedical Engineering, Wenzhou Medical University, Wenzhou, 325000, PR China
† Electronic supplementary information (ESI) available. See DOI: 10.1039/c9ce00039a
‡ These authors contributed equally to this work.

facile synthetic method to produce Pt-based alloys with well-defined hollow/porous structures is still highly desired.

Herein, we reported a novel strategy for the fabrication of Pt–Cu alloy tetradecahedrons (Pt–Cu TNs) with a hollow interior and a porous surface structure. More specifically, Cu_2O particles with a regular shape were used as the foundation template. As H^+ species were introduced into the solution, Cu_2O particles rapidly produced Cu atoms for the disproportionation reaction. Meanwhile, the Pt precursor was instantaneously reduced by Cu atoms. Owing to the quick reduction, the morphology was retained well. The novelty of our approach is described as follows: (I) our catalyst is produced in an aqueous solution and at an ambient temperature, which are environmentally friendly and meet the economical requirements in the actual production. (II) The shape of the sacrificial template (Cu_2O) provides controllability over the size and the shape of final hollow products; Cu_2O with various shapes and sizes can be easily synthesized. (III) No additional reducing agent is introduced. (IV) The thickness of the shell and the component ratio in Pt–Cu TNs can be conveniently regulated (more details have been shown in the Results and discussion section). (V) This versatile strategy may open the avenue to the rational design of bimetallic Cu–M (M: Pd, Au, Co, *etc.*) hollow structures for various applications.

Experimental

Reagents and chemicals

Copper(II) chloride dehydrate ($CuCl_2{\cdot}2H_2O$), chloroplatinic acid hexahydrate ($H_2PtCl_6{\cdot}6H_2O$), potassium hexachloroplatinate (K_2PtCl_6), and sodium hydroxide (NaOH) were purchased from Shanghai McLean Biochemical Technology Co., Ltd. Polyvinylpyrrolidone (PVP, K29-32) and ascorbic acid (AA) were purchased from Aladdin Reagent Co., Ltd. Pt black was purchased from Johnson Matthey Chemicals Ltd. Other reagents were of analytical grade and used without further purification.

Preparation of Cu_2O tetradecahedrons

Cu_2O tetradecahedrons were synthesized according to a previously reported procedure.[33] Briefly, one mmol of $CuCl_2{\cdot}2H_2O$ and 4.5 g of PVP were dissolved into 100 mL of deionized water. Then, 10 mL aqueous solution containing 20 mmol NaOH was added dropwise into the above solution with continuous stirring. After 0.5 h, 10 mL aqueous solution containing 6 mmol of AA was further added into the mixed solution. Finally, the solution was aged for at least 3 h. The whole procedure was carried out in a water bath at 55 °C. The resulting products were washed with deionized water by centrifuging repeatedly to remove the residual ions and polymer and then dried in vacuum at 50 °C for further use (for 5 h).

Preparation of hollow platinum–copper tetradecahedrons (Pt–Cu TNs)

To prepare Pt–Cu TNs, 0.17 mmol of Cu_2O tetradecahedrons was dispersed in 250 mL of deionized water with 0.05 g PVP by ultrasonic vibration for 30 min. Then, 0.5 mL of 50 mM H_2PtCl_6 was sequentially dropped into the above solution. The colour of the solution turned from orange to dark black in 5 minutes, indicating the formation of Pt–Cu TNs. Finally, the resulting products were centrifuged and washed with deionized water several times. Finally, the products were dried in vacuum at 50 °C for further use and characterization (for 5 h).

Physical characterization

The morphology and the surface structure of the products were characterized by a JEOL JEM-2100F transmission electron microscope (TEM) and a JSM-2010 scanning electron microscope (SEM). High-resolution TEM (HRTEM), high angle annular dark-field scanning transmission electron microscopy (HAADF-STEM), and energy dispersive X-ray (EDX) elemental mapping were performed on a JEOL JSM-7600F microscope equipped with an EDAX X-ray detector. The samples were prepared by dropping the catalyst dispersion in deionized water on a carbon film coated on a molybdenum grid (300 mesh). The composition and the crystal structure of the products were investigated by a Leeman inductively coupled plasma atomic emission spectrometer (ICP-AES), a model D/max-rC X-ray diffractometer (XRD) and an AXIS ULTRA DLD X-ray photoelectron spectroscope (XPS). Nitrogen adsorption–desorption isotherm (BET) experiment was performed on a Micromeritics ASAP 2020 instrument.

Electrochemical measurements

All electrochemical experiments were performed in an all-Teflon three-electrode cell by using a CHI 660 E electrochemical analyser (CH Instruments, Shanghai, Chenhua Co.). In particular, a catalyst-modified glassy carbon electrode (3 mm diameter, 0.07 cm^2) was used as the working electrode, a platinum wire was used as the auxiliary electrode and an Ag/AgCl electrode was used as the reference electrode. The working electrodes were prepared as follows: the catalyst ink was prepared by sonicating the catalyst powder in deionized water at 2 mg mL^{-1} for at least 30 min. Then, the catalyst ink was irradiated with UV irradiation (185 and 254 nm) in air for 4 h to remove the capping agents (*i.e.*, PVP). Then, 6 μL of the resulting suspension was dropped onto the surface of the glassy carbon electrode. After drying, 2 μL of the Nafion solution (5 wt%) was laid on the surface of the modified electrode and dried again. Cyclic voltammetry (CV) measurements were carried out in an N_2-saturated 0.5 M H_2SO_4 aqueous solution. The methanol oxidation reaction (MOR) experiments were performed in an N_2-saturated 0.5 M H_2SO_4 solution with 1 M CH_3OH.

Results and discussion

Characterization of hollow Pt–Cu alloy tetradecahedrons

For the synthesis of hollow Pt–Cu TNs, the starting template Cu_2O was initially synthesized by an aqueous reduction method reported in literature.[33] The transmission electron

microscopy (TEM, Fig. 1a) and scanning electron microscopy (SEM, Fig. 1b) images of the as-prepared Cu_2O present uniform tetradecahedral morphology with an average size of ~400 nm. In Fig. 1a, two different shapes (quadrate and hexagon) are observed owing to different visual angles. TEM observation reveals a solid internal structure. SEM image shows Cu_2O templates with smooth surfaces (Fig. 1b). The X-ray diffraction (XRD) pattern confirmed the formation of the Cu_2O phase (Fig. 1c). Subsequently, the obtained Cu_2O tetradecahedrons were ultrasonically dispersed in aqueous solutions. Then, an H_2PtCl_6 solution was added dropwise into the above Cu_2O solution. The products could be quickly generated in five minutes. According to the XRD pattern, Pt–Cu TNs display the characteristics of an fcc structure (Fig. 1d). The diffraction peaks of Pt–Cu TNs were located between those of fcc Cu (JCPDS no. 04-0836) and fcc Pt (JCPDS no. 04-0802). Moreover, no other characteristic peaks such as the peaks of pure Pt, Cu or their oxides were observed, indicating the formation of the Pt–Cu alloy. To study the surface electronic state, X-ray photoelectron spectroscopy (XPS) was performed. As shown in Fig. S1,† the Pt 4f binding energy ($4f_{5/2}$ = 72.83 eV; $4f_{7/2}$ = 69.2 eV) of Pt–Cu TNs negatively shifts as compared to that of the standard bulk Pt ($4f_{5/2}$ = 73.46 eV; $4f_{7/2}$ = 70.15 eV).[34] The negative shift of the Pt 4f binding energy was due to the different electronegativities of Pt (2.28) and Cu (1.90), which resulted in the electron withdrawal from Cu to Pt atoms in their alloy. The abundant electrons of Pt in Pt–Cu TNs may hinder the electron donation from CO and therefore may improve the anti-CO adsorption and the stability in MOR.[35,36] N_2 adsorption–desorption analysis showed that Pt–Cu TNs have a high surface area of 69 $m^2\ g^{-1}$. The isotherm exhibited type IV behaviors, indicating the presence of a porous structure in Pt–Cu TNs (Fig. S2†).[37,38]

The morphology and structure of Pt–Cu TNs were further characterized by SEM and TEM. As indicated by the SEM image in Fig. 2a, Pt–Cu TNs have uniform size distribution. The inset image shows that Pt–Cu TNs have a hollow core. The TEM image of the products displays rough surfaces with a significantly hollow core of about 375 nm and a thin shell of about 25 nm. These factors may facilitate the mass transfer of reactants between their inner space and the surrounding medium. Please note that various shapes were observed owing to different viewing angles, as indicated in Fig. 2b. A hexagon-shaped structure can be observed from the side view, while a quadrate shape is observed from the top view. Fig. 2c and d show the high-resolution TEM (HRTEM) images of Pt–Cu TNs. As observed, the rough surfaces display numerous atomic steps, edges and corner atoms marked by the red line, which can endow Pt–Cu TNs with more exposed active sites. A continuous lattice fringe pattern is also observed with a fringe interval of *ca.* 0.216 nm. It should be noted that the fringe interval was slightly smaller than that of the (111) facet of the face-centered cubic (fcc) Pt crystal (0.226 nm). The result not only confirmed that Pt–Cu TNs have dominant (111) facets but also indicated the formation of the Pt–Cu alloy.[39] In addition, the selected-area electron diffraction (SAED) image shows that Pt–Cu TNs are polycrystalline (Fig. S3, ESI†). To study the composition of Pt–Cu TNs, EDX and ICP-AES techniques were used. According to the EDX results (Fig. S4†), the Pt : Cu atomic ratio was estimated to be 48.6 : 51.4, which was in good agreement with the result from ICP-AES analysis (49.7 : 50.3). The EDX elemental mapping and EDX line scanning profiles were obtained to get more details of the elemental distribution in Pt–Cu TNs. The elemental

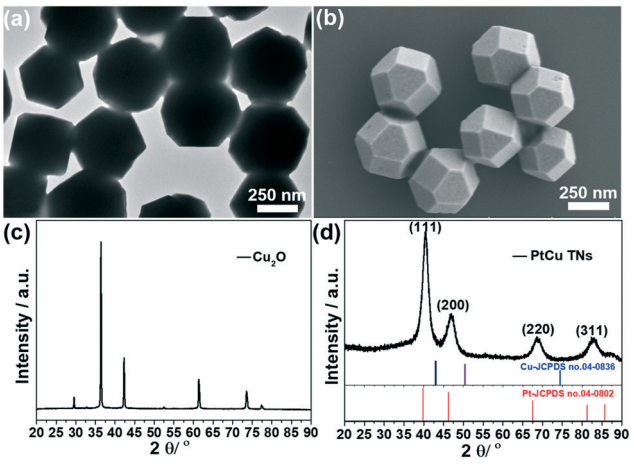

Fig. 1 (a) TEM and (b) SEM images of Cu_2O tetradecahedrons; (c) XRD pattern of Cu_2O tetradecahedrons; (d) XRD pattern of Pt–Cu TNs.

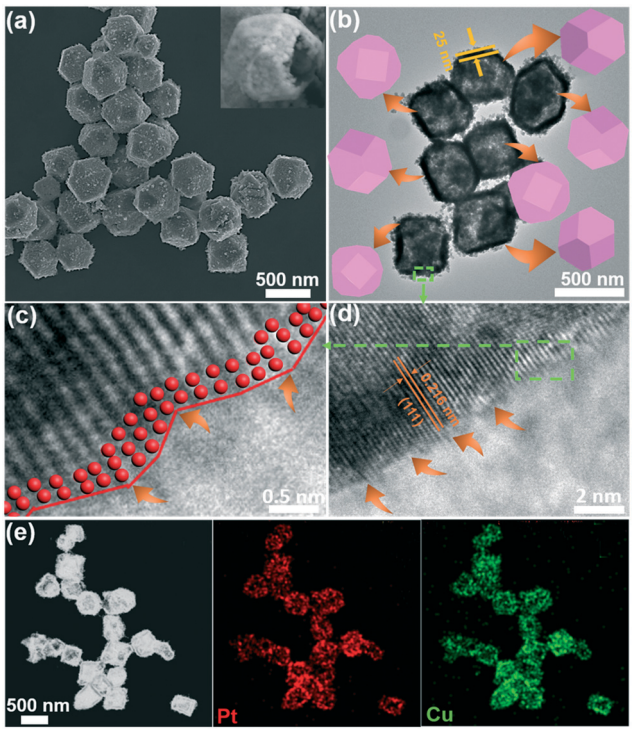

Fig. 2 (a) SEM image of Pt–Cu TNs. Inset: SEM image of an individual Pt–Cu TN with a broken shell; (b) TEM image and geometric models of an individual Pt–Cu TN imaged at different visual angles; (c and d) magnified HRTEM images of Pt–Cu TNs; (e) HAADF-STEM image and EDX elemental mapping patterns of Pt–Cu TNs.

mapping results (Fig. 2e) showed that Pt and Cu atoms were homogenously distributed and highly overlapped, suggesting a high alloying degree for Pt–Cu TNs. Furthermore, the EDX line scanning profiles demonstrated that Pt–Cu TNs are Cu-rich (Fig. S5†), which was consistent with the EDX and ICP-AES results.

Formation mechanism of hollow Pt–Cu TNs

To investigate the formation mechanism of Pt–Cu TNs, time sequential evolution experiments were carried out (Fig. 3). A completely solid nanostructure was observed before the reaction, which transformed into a mesoporous and hollow structure in 1 min. Meanwhile, the surface of the particle became more and more rough. After 5 min, an entirely hollow structure appeared.

In addition, control experiments were carried out to confirm the growth mechanism of Pt–Cu TNs. The roles of H^+ and PVP species in the reaction were primarily examined. When H_2PtCl_6 was replaced by K_2PtCl_6, no significant reaction was observed. Meanwhile, sediments could be clearly observed without PVP's addition in the reaction process. Therefore, we expect that H^+ and PVP acted as the inductive agent and the stabilizing agent, respectively.

$$Cu_2O + 2H^+ = Cu + Cu^{2+} + H_2O \quad (1)$$

$$2Cu + PtCl_6^{2-} = Pt + 2Cu^{2+} + 6Cl^- \quad (2)$$

$$3Cu_2O + 6H^+ + PtCl_6^{2-} = Cu + Pt + 5Cu^{2+} + 3H_2O + 6Cl^- \quad (3)$$

Based on the experimental results, we proposed a possible mechanism for the formation of Pt–Cu TNs, as shown in Fig. 4. It is well-known that Cu^+ easily exerts a disproportionation reaction at room temperature (eqn (1)). With the addition of H_2PtCl_6, the disproportionation reaction was immediately triggered. Due to the occurrence of the replacement reaction, Cu atoms were rapidly oxidized by $PtCl_6^{2-}$ *in situ* (eqn (2)) because the standard reduction potential of $PtCl_6^{2-}$/Pt (0.74 V *vs.* RHE) is significantly more positive than that of Cu^{2+}/Cu (0.34 V *vs.* RHE). In addition, their morphology and structure were retained owing to the *in situ* reduction. To understand the mechanism more easily, the overall reaction (eqn (3)) is presented based on the reactions given in eqn (1) and (2). The formation of one Pt atom consumed three Cu_2O, which resulted in redundant vacancies on the surface of Pt–Cu TNs, as verified by BET. Moreover, one Pt atom was generated along with one Cu atom, coinciding with EDX and ICP-AES results. Overall, Cu_2O was gradually replaced by H_2PtCl_6, forming the Pt–Cu alloy on the surface and generating the hollow structure.

Moreover, we tried to regulate the Pt : Cu ratio in Pt–Cu TNs. In the experiment, we replaced H_2PtCl_6 with K_2PtCl_6 and then, excess H^+ was added to ensure the completion of the reaction. According to EDX results (Fig. S6†), the Pt proportion in Pt–Cu TNs increased with continuous addition of K_2PtCl_6. Amazingly, we found that the thickness of the shell also increased until the hollow structure disappeared (Fig. 5). This showed that we could conveniently control the thickness of Pt–Cu TNs.

Furthermore, when the ratio of K_2PtCl_6 with Cu_2O in the reaction solution was adjusted to below 1 : 2, the copper atoms could not be completely consumed. The remaining Cu atoms alloyed with the Pt atoms *in situ* with various ratios

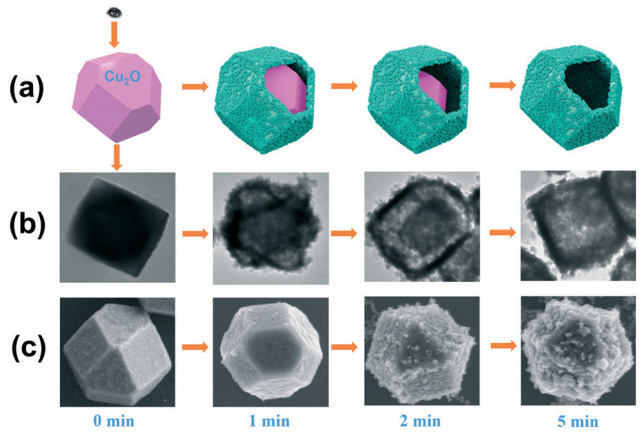

Fig. 3 (a) Geometric models, (b) TEM images and (c) SEM images of Pt–Cu TNs collected at different growth stages: 0 min, 1 min, 2 min, 5 min.

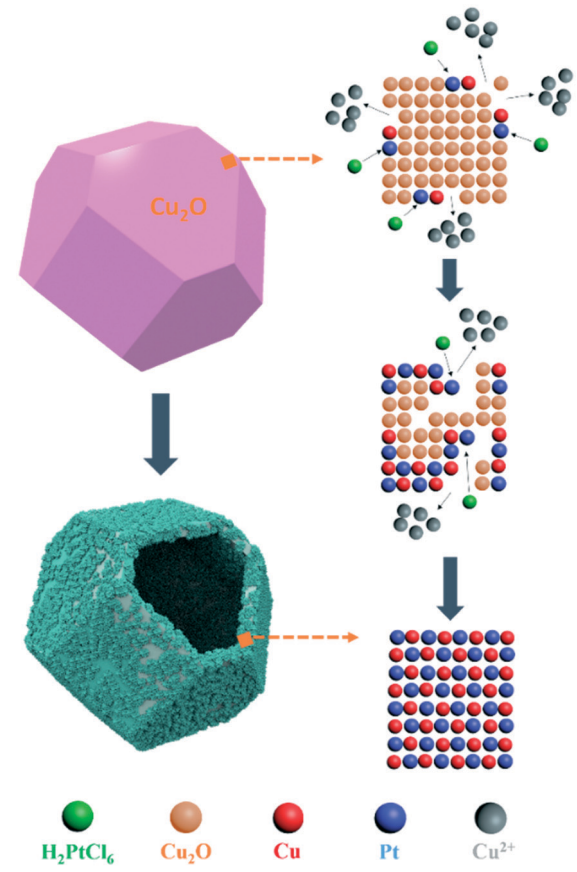

Fig. 4 Schematic illustration for the formation of Pt–Cu TNs.

(Fig. 5a–c). Cu_2O in the middle part progressively collapsed due to the addition of excess H^+. Finally, a hollow alloy structure was formed. However, as the ratio of K_2PtCl_6 with Cu_2O in the reaction solution reached 1 : 2 ($2Cu_2O + 4H^+ + PtCl_6^{2+} = 4Cu^{2+} + Pt + 2H_2O + 6Cl^-$), the product displayed a porous Pt tetradecahedron (Fig. 5d) because the Cu atoms were completely consumed *in situ* during the reaction.

Catalytic activity

The electrochemical properties of Pt–Cu TNs were first investigated by cyclic voltammetry (CV) in a 0.5 M H_2SO_4 solution (Fig. 6a). By measuring the adsorption charge of hydrogen, ECSA of Pt–Cu TNs was determined to be 42.0 $m^2\ g_{Pt}^{-1}$, which was much higher than the value of Pt black (16.9 $m^2\ g^{-1}$); this may be ascribed to the hollow and porous structure. Then, the methanol oxidation reaction (MOR) was applied to evaluate the electrocatalytic performance of Pt–Cu TNs and Pt black. More specifically, the electrocatalytic performance of these catalysts was investigated by CV in an N_2-saturated solution containing 1 M CH_3OH and 0.5 M H_2SO_4 using the same Pt loading. Compared with the observations for Pt black, the oxidation peak potential (Fig. 6b) and the onset oxidation potential of methanol (left inset pattern in Fig. 6b) on Pt–Cu TNs negatively shifted *ca.* 51.8 and 24.0 mV, indicating improved reaction kinetics. Furthermore, the mass activity (*i.e.*, the currents are normalized to the metal mass) and the specific activity (*i.e.*, the current is normalized to ECSA of electrocatalysts) are generally taken as indexes to evaluate the activity of electrocatalysts. As shown in Fig. 6b and c, the peak current densities of mass activity (0.88 A mg_{Pt}^{-1}, Fig. 6b) and specific activity (2.5 mA cm^{-2}, Fig. 6c) of Pt–Cu TNs are

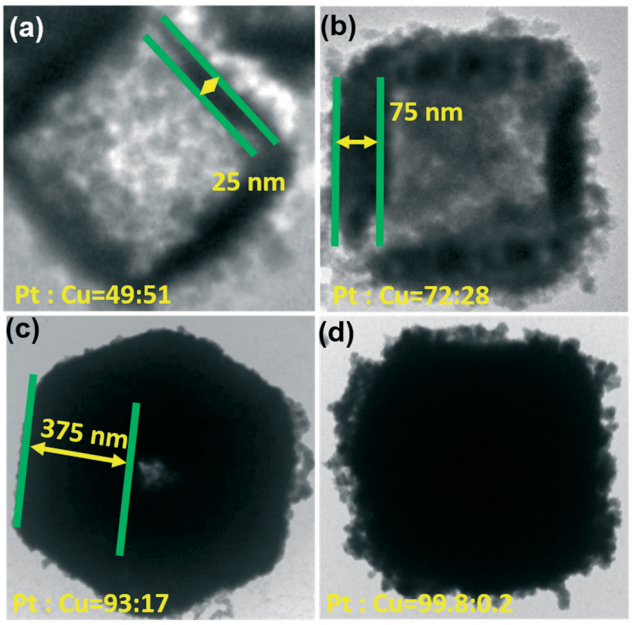

Fig. 5 (a–d) TEM images of Pt–Cu TNs tailored by different amounts of K_2PtCl_6.

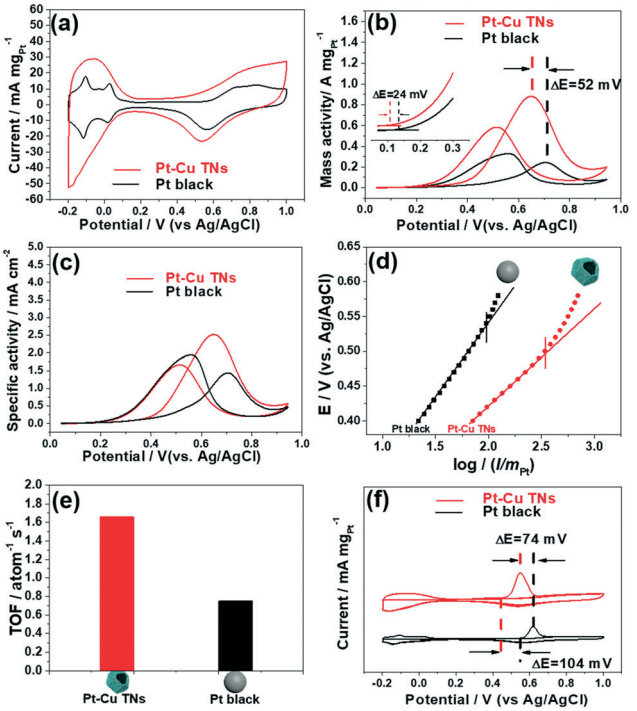

Fig. 6 (a) CVs in N_2-saturated 0.5 M H_2SO_4 solution; (b) Pt mass-normalized CVs in 1 M CH_3OH and 0.5 M H_2SO_4; (c) ESCA normalized CVs in 1 M CH_3OH and 0.5 M H_2SO_4; (d) Tafel plots of log *I vs. E* for the MOR in the electrochemical control area; (e) TOF of related catalysts; (f) CO stripping voltammograms in 0.5 M H_2SO_4 solution. Scan rate: 50 mV s^{-1}.

3.7 and 1.8 times higher than those of Pt black (0.24 A mg^{-1} and 1.4 mA cm^{-2}, respectively). Significantly, compared with previously reported catalysts (shown in Table S1†), Pt–Cu TNs have better activity. Then, as shown by the Tafel plots of the catalysts in Fig. 6d, both curves exhibit a good linear relationship in the lower current region. Furthermore, Pt–Cu TNs displayed a higher output current than Pt black under the same output voltage. These results suggested that MOR occurring at Pt–Cu TNs has a faster kinetic rate. The TOF value, which gives the moles of methanol molecules converted per Pt surface site per second, was further calculated according to the equation TOF = i_k/neN_s.[40] In Fig. 6e, the TOF results of Pt–Cu TNs display a higher value than those of Pt black, which verifies the improved electrocatalytic efficiency of Pt–Cu TNs. Clearly, the as-prepared Pt–Cu TNs showed competitive electrocatalytic activity for MOR.

The outstanding enhanced electro-catalytic activity of Pt–Cu TNs can be ascribed to the following aspects: (1) the hollow structure provides a high specific surface area (as verified by BET) and easy access for reactants.[41,42] (2) The rough surfaces possess a large number of atomic steps, edges and corner atoms and offer abundant catalytic sites.[34] (3) The alloy effect (ensemble effect) between Pt and Cu in Pt–Cu bimetallic nanostructures. According to recent experimental and theoretical results from Henkelman's and Mullins' groups, the ensemble effect can significantly change the dehydrogenation selectivity of alcohol, which in turn changes the final

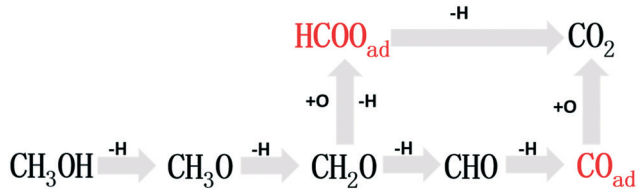

Scheme 1 Methanol dehydrogenation routes.

products of oxidation.[43–46] Similarly, the ensemble effect has significant influence on MOR. It is well-known that MOR in an acidic solution involves two main steps. First, the adsorbed methanol molecule undergoes progressive dehydrogenation on the catalyst surface to produce a CO intermediate and $HCOO^-$ intermediates. Then, the intermediates are finally oxidized to CO_2 (as shown in Scheme 1).[47] In Pt–Cu TNs, significantly, the electron binding energy of Pt was lowered by alloying with Cu, as verified by XPS, which promoted the cleavage of the C–H bond in MOR.[48] The oxygenated species produced by Cu facilitated methanol oxidation to CO_2 *via* $HCOO^-$ intermediates instead of CO, which protected the materials from CO poisoning.[38]

In addition, the ratio of the forward oxidation current peak (I_f) to the reverse current peak (I_b) for Pt–Cu TNs (1.52) was found to be much higher than that for Pt black (0.74), indicating better poison tolerance of CO.[49,50] To further evaluate the poisoning effect of CO, CO stripping cyclic voltammetry for Pt–Cu TNs in 0.5 M H_2SO_4 solution was performed. In Fig. 6f, we observe that the onset potential and the peak potential of CO anodic oxidation on Pt–Cu TNs negatively shift *ca.* 103.9 and 74.2 mV as compared to those of Pt black. The above results indicated that Pt–Cu TNs have weaker CO adsorption and better CO tolerance than Pt black, which may be important reasons for the enhanced electrocatalytic stability.

Thus, the stability of Pt–Cu TNs and Pt black towards MOR was further studied by using chronoamperometry in a solution containing 0.5 M H_2SO_4 and 1 M CH_3OH at 0.65 V (Fig. S7†). After 3000 s, the oxidation currents of methanol on Pt–Cu TNs and Pt black decreased to 16.2% and 4.8% of their initial values, respectively. This indicated that Pt–Cu TNs are more stable as an electrocatalyst for MOR. The improved stability can be attributed to the hollow structure, better CO tolerance and the electrochemical dealloying effect. The hollow structure could inhibit aggregation and Ostwald ripening during the catalytic process. Furthermore, the dealloying effect appeared after multiple catalytic cycles, which restructured the Cu atoms on the surfaces of Pt–Cu TNs to become stable for oxidation.[51]

Conclusions

In summary, we developed a novel, facile and efficient synthetic strategy to synthesize Pt–Cu TNs with a hollow structure (~375 nm) and rough surfaces. The structural parameters of Pt–Cu TNs, including the size and thickness of the shell, and the ratio of Pt/Cu could be controlled by altering the experimental conditions. The formation mechanism of such a hollow structure of Pt–Cu TNs was proposed. Benefiting from the unique structure and the synergetic effect between Pt and Cu, Pt–Cu TNs exhibited significantly improved electrocatalytic activity and durability towards MOR as compared to a Pt black catalyst. It is believed that this versatile strategy may open an avenue for the rational design of bimetallic Cu–M (M: Pd, Au, Co, *etc.*) hollow structures for various applications.

Conflicts of interest

There are no conflicts to declare.

Acknowledgements

This research was sponsored by the National Natural Science Foundation of China (21605116, 21875112 and 51672193), Public Projects of Zhejiang Province (2017C33193), the Natural Science Foundation of Zhejiang Province (LQ18B030001), Public Projects of Wenzhou (Y20160065, Y20160067), Wenzhou government's startup fund (WIBEZD2014004-02), Wenzhou leading talent innovation and entrepreneurship project (RX2016005).

References

1 K. Mikkelsen, B. Cassidy, N. Hofstetter, L. Bergquist, A. Taylor and D. A. Rider, *Chem. Mater.*, 2014, **26**, 6928–6940.
2 G. Fu, X. Yan, Z. Cui, D. Sun, L. Xu, Y. Tang, J. B. Goodenough and J.-M. Lee, *Chem. Sci.*, 2016, **7**, 5414–5420.
3 H. Liu, J. Qu, Y. Chen, J. Li, F. Ye, J. Y. Lee and J. Yang, *J. Am. Chem. Soc.*, 2012, **134**, 11602–11610.
4 J.-J. Fan, Y.-J. Fan, R.-X. Wang, S. Xiang, H.-G. Tang and S.-G. Sun, *J. Mater. Chem. A*, 2017, **5**, 19467–19475.
5 F. Ren, C. Wang, C. Zhai, F. Jiang, R. Yue, Y. Du, P. Yang and J. Xu, *J. Mater. Chem. A*, 2013, **1**, 7255–7261.
6 J. Sun, H. Ma, H. Jiang, L. Dang, Q. Lu and F. Gao, *J. Mater. Chem. A*, 2015, **3**, 15882–15888.
7 W. Yuan, Y. Cheng, P. K. Shen, C. M. Li and S. P. Jiang, *J. Mater. Chem. A*, 2015, **3**, 1961–1971.
8 G. Xu, R. Si, J. Liu, L. Zhang, X. Gong, R. Gao, B. Liu and J. Zhang, *J. Mater. Chem. A*, 2018, **6**, 12759–12767.
9 T. Li, Y. Wang, Y. Tang, L. Xu, L. Si, G. Fu, D. Sun and Y. Tang, *Catal. Sci. Technol.*, 2017, **7**, 3355–3360.
10 H. Sun, L. Qi, X. Jiang, G. Fu, L. Xu, D. Sun, Z. Gu and Y. Tang, *New J. Chem.*, 2017, **41**, 8812–8817.
11 Y. Bing, H. Liu, L. Zhang, D. Ghosh and J. Zhang, *Chem. Soc. Rev.*, 2010, **39**, 2184–2202.
12 G. Fu, R. Ma, X. Gao, Y. Chen, Y. Tang, J.-M. Lee and T. Lu, *Nanoscale*, 2014, **6**, 12310–12314.
13 C. Cui, L. Gan, M. Heggen, S. Rudi and P. Strasser, *Nat. Mater.*, 2013, **12**, 765–771.
14 C. Luan, Q.-X. Zhou, Y. Wang, Y. Xiao, X. Dai, X.-L. Huang and X. Zhang, *Small*, 2017, **13**, 1702617–170261729.
15 G. Fu, H. Liu, N. You, J. Wu, D. Sun, L. Xu, Y. Tang and Y. Chen, *Nano Res.*, 2016, **9**, 755–765.

16 F. Wen, Y. Zhang, J. Tan, Z. Zhou, M. Zhu, S. Yin and H. Wang, *J. Electroanal. Chem.*, 2018, **822**, 10–16.
17 Q. Zhang, D. Liang, H. Cui, J. Zhai, Z. Wei and Q. Li, *Appl. Surf. Sci.*, 2014, **308**, 113–120.
18 Q. Chen, Z. Cao, G. Du, Q. Kuang, J. Huang, Z. Xie and L. Zheng, *Nano Energy*, 2017, **39**, 582–589.
19 A. Oh, Y. J. Sa, H. Hwang, H. Baik, J. Kim, B. Kim, S. H. Joo and K. Lee, *Nanoscale*, 2016, **8**, 16379–16386.
20 G. Fu, M. Gong, Y. Tang, L. Xu, D. Sun and J.-M. Lee, *J. Mater. Chem. A*, 2015, **3**, 21995–21999.
21 T. Yang, H. Zhu, M. Wan, L. Dong, M. Zhang and M. Du, *Chem. Commun.*, 2016, **52**, 990–993.
22 T. Zhang, S.-C. Li, W. Zhu, Z.-P. Zhang, J. Gu and Y.-W. Zhang, *Nanoscale*, 2017, **9**, 1154–1165.
23 G. Fu, Q. Zhang, J. Wu, D. Sun, L. Xu, Y. Tang and Y. Chen, *Nano Res.*, 2015, **8**, 3963–3971.
24 S. Chen, F. Wu, L. Shen, Y. Huang, S. K. Sinha, V. Srot, P. A. van Aken, J. Maier and Y. Yu, *ACS Nano*, 2018, **12**, 7018–7027.
25 H. P. Liang, H. M. Zhang, J. S. Hu, Y. G. Guo, L. J. Wan and C. L. Bai, *Angew. Chem., Int. Ed.*, 2004, **43**, 1540–1543.
26 J. W. Hong, S. W. Kang, B.-S. Choi, D. Kim, S. B. Lee and S. W. Han, *ACS Nano*, 2012, **6**, 2410–2419.
27 H. Zhang, M. Jin, H. Liu, J. Wang, M. J. Kim, D. Yang, Z. Xie, J. Liu and Y. Xia, *ACS Nano*, 2011, **5**, 8212–8222.
28 K. Jiang, Q. Shao, D. Zhao, L. Bu, J. Guo and X. Huang, *Adv. Funct. Mater.*, 2017, **27**, 1700830–1700836.
29 X. Yang, L. T. Roling, M. Vara, A. O. Elnabawy, M. Zhao, Z. D. Hood, S. Bao, M. Mavrikakis and Y. Xia, *Nano Lett.*, 2016, **16**, 6644–6649.
30 S. Luo and P. K. Shen, *ACS Nano*, 2016, **11**, 11946–11953.
31 J. Ding, L. Bu, S. Guo, Z. Zhao, E. Zhu, Y. Huang and X. Huang, *Nano Lett.*, 2016, **16**, 2762–2767.
32 U. Aslam and S. Linic, *Chem. Mater.*, 2016, **28**, 8289–8295.
33 D. F. Zhang, H. Zhang, L. Guo, K. Zheng, X. D. Han and Z. Zhang, *J. Mater. Chem.*, 2009, **19**, 5220–5225.
34 R. Zhao, Y. Liu, C. Liu, G. Xu, Y. Chen, Y. Tang and T. Lu, *J. Mater. Chem. A*, 2014, **2**, 20855–20860.
35 Y. Zhao, J. Liu, C. Liu, F. Wang and Y. Song, *ACS Catal.*, 2016, **6**, 4127–4134.
36 M. Watanabe, A. Yimin Zhu and H. Uchida, *J. Phys. Chem. B*, 2000, **104**, 1762–1768.
37 L. Zhang, Q. Sui, T. Tang, Y. Chen, Y. Zhou, Y. Tang and T. Lu, *Electrochem. Commun.*, 2013, **32**, 43–46.
38 K. Eid, H. Wang, P. He, K. Wang, T. Ahamad, S. M. Alshehri, Y. Yamauchi and L. Wang, *Nanoscale*, 2015, **7**, 16860–16866.
39 M. Gong, G. Fu, Y. Chen, Y. Tang and T. Lu, *ACS Appl. Mater. Interfaces*, 2014, **6**, 7301–7308.
40 X. Zhang, S. Tian, W. Yu, B. Lu, T. Shen, L. Xu, D. Sun, S. Zhang and Y. Tang, *CrystEngComm*, 2018, **20**, 4277–4282.
41 X. J. Liu, C. H. Cui, H. H. Li, Y. Lei, T. T. Zhuang, M. Sun, M. N. Arshad, H. A. H. M. Albar, T. R. Sobahi and S. H. Yu, *Chem. Sci.*, 2015, **6**, 3038–3043.
42 L. Wang and Y. Yamauchi, *J. Am. Chem. Soc.*, 2013, **135**, 16762–16765.
43 H. Li and G. A. Henkelman, *J. Phys. Chem. C*, 2017, **121**, 27504–27510.
44 H. Li, K. Shin and G. Henkelman, *J. Chem. Phys.*, 2018, **149**, 174705–174713.
45 H. Li, E. J. Evans, Jr., C. B. Mullins and G. Henkelman, *J. Phys. Chem. C*, 2018, **122**, 22024–22032.
46 E. J. Evans, Jr., H. Li, W.-Y. Yu, G. M. Mullen, G. Henkelman and C. B. Mullins, *Phys. Chem. Chem. Phys.*, 2017, **19**, 30578–30589.
47 C. Poochai, W. Veerasai, E. Somsook and S. Dangtip, *Electrochim. Acta*, 2016, **222**, 1243–1256.
48 G. Fu, X. Yan, Z. Cui, D. Sun, L. Xu, Y. Tang, J. B. Goodenough and J.-M. Lee, *Chem. Sci.*, 2016, **7**, 5414–5420.
49 Y. Liao, G. Yu, Y. Zhang, T. Guo, F. Chang and C. J. Zhong, *J. Phys. Chem. C*, 2016, **120**, 10476–10484.
50 M. Yang, Q. Cai, C. Liu, R. Wu, D. Sun, Y. Chen, Y. Tang and T. Lu, *J. Mater. Chem. A*, 2014, **2**, 13738–13743.
51 M. Xiao, S. Li, X. Zhao, J. Zhu, M. Yin, C. Liu and W. Xing, *ChemCatChem*, 2014, **6**, 2825–2831.